

Article

Adsorption Behavior of Organoarsenicals over MnFe₂O₄-Graphene Hybrid Nanocomposite: The Role of Organoarsenic Chemical Structures

Binxian Gu ^{1,2}, Haijie Zhang ¹, Meng Ye ¹, Ting Zhou ¹, Jianjian Yi ¹  and Qingsong Hu ^{1,*} 

¹ College of Environmental Science and Engineering, Yangzhou University, 196 West Huayang Road, Yangzhou 225127, China; bxgu@yzu.edu.cn (B.G.); mz120211210@stu.yzu.edu.cn (H.Z.); mz120221245@stu.yzu.edu.cn (M.Y.); mz120221241@stu.yzu.edu.cn (T.Z.); jjyi@yzu.edu.cn (J.Y.)

² Jiangsu Collaborative Innovation Center for Solid Organic Waste Resource Utilization, Nanjing 210095, China

* Correspondence: huqs@yzu.edu.cn

Abstract: As a kind of emerging contaminant, organoarsenic compounds have drawn wide concern because of their considerable solubilities in water, and the highly toxic inorganic arsenic species formed during their biotic and abiotic degradation in the natural environment. Thus, the effective removal and studying of the adsorption mechanism of organoarsenic compounds are of significant urgency. In this work, MnFe₂O₄ and MnFe₂O₄/graphene were prepared through a facile solvothermal method. From the results of the Transmission Electron Microscope (TEM) characterization, it can be found that MnFe₂O₄ nanoparticles were uniformly distributed on the surface of the graphene. And the specific surface area of the MnFe₂O₄/graphene was about 146.39 m² g⁻¹, much higher than that of the MnFe₂O₄ (86.15 m² g⁻¹). The interactions between organoarsenic compounds and adsorbents were conducted to study their adsorption behavior and mechanism. The maximum adsorption capacities of MnFe₂O₄/graphene towards p-arsanilic acid (p-ASA) and roxarsone (ROX) were calculated to be 22.75 and 30.59 mg g⁻¹. Additionally, the ionic strength, negative ions, and humus were introduced to investigate the adsorption performance of organoarsenic compounds. Electrostatic adsorption and surface complexation are the primary adsorption mechanisms on account of X-ray photoelectron spectroscopy (XPS) and the Fourier-transform infrared spectroscopy (FT-IR) analysis. This research extends the knowledge into studying the interaction between organoarsenic species and hybrid nanomaterials in the natural environment.

Keywords: MnFe₂O₄; graphene; adsorption; p-arsanilic acid; roxarsone



Citation: Gu, B.; Zhang, H.; Ye, M.; Zhou, T.; Yi, J.; Hu, Q. Adsorption Behavior of Organoarsenicals over MnFe₂O₄-Graphene Hybrid Nanocomposite: The Role of Organoarsenic Chemical Structures. *Materials* **2023**, *16*, 7636. <https://doi.org/10.3390/ma16247636>

Academic Editor: Alexander N. Obraztsov

Received: 23 November 2023

Revised: 9 December 2023

Accepted: 12 December 2023

Published: 14 December 2023



Copyright: © 2023 by the authors. Licensee MDPI, Basel, Switzerland. This article is an open access article distributed under the terms and conditions of the Creative Commons Attribution (CC BY) license (<https://creativecommons.org/licenses/by/4.0/>).

1. Introduction

Water contaminated with arsenic (As) presents a pressing and formidable challenge due to its high toxicity, bioaccumulation potential, and carcinogenic properties [1]. Long-term exposure to wastewater containing arsenic can lead to a range of diseases, including neurological, dermatological, and endocrine disorders [2]. The detrimental effects of arsenic contamination may take over a decade to become apparent, especially at low exposure levels. Therefore, when arsenic contamination arises in water, it has the potential to enter the human body via the food chain or biogeochemical cycle, posing a severe threat to human health [3].

The existence of arsenic in nature displays two forms: organic arsenic and inorganic arsenic. Organic arsenic compounds contain aromatic organoarsenicals and diverse methylated arsenic. In contrast, inorganic arsenic comprises arsenate species (As(V)) and arsenite species (As(III)). Notably, aromatic organoarsenicals, such as p-arsanilic acid (p-ASA) and roxarsone (ROX), have been widely employed in agriculture for decades [4]. They serve the purpose of promoting livestock growth and preventing the proliferation of parasites. These organoarsenicals show limited adsorption and conversion within animals and are primarily

excreted through metabolic processes [5]. However, it is crucial to note that organoarsenicals display minimal toxicity and undergo decomposition in soil. They can eventually undergo biotransformation processes, leading to their conversion into various more mobile and toxic inorganic arsenic compounds [6]. In the southern part of China's Pearl River Delta, p-ASA was detected at 12 µg/kg in the surface soil surrounding pig farms, indicating increased arsenic levels compared to the local background [7]. Additionally, chicken and pig manure in China contained total arsenic ranging from 8.10×10^5 to 5.7×10^6 and from 0.9×10^5 to 2.5×10^7 kg per year [8]. Long-term exposure to arsenic-contaminated drinking water may result in endemic arsenicosis and fatal cancers [9]. Therefore, it is crucial and urgent to remove organic arsenic-contaminated water from the source before its conversion to highly toxic inorganic arsenic in order to prevent arsenic migration and control environmental risks.

Currently, the use of organoarsenicals in agriculture and livestock farming has had a significant environmental impact. The removal of p-ASA and ROX from the environment has become a focal point of research in the environmental field. Disappointingly, research on the removal of organoarsenicals is relatively scarce compared to that on inorganic arsenic, and the development of suitable removal methods is crucial for controlling organic arsenic pollution in livestock [10]. At present, several removal techniques have been proposed, including photodecomposition [5], biodegradation [11], and adsorption [11,12]. Among these methods, adsorption shows the advantages of high efficiency and low cost [13]. Various natural and synthetic adsorbents have been studied for arsenic sorption from water bodies [14]. As a consequence, the development of low-cost, high-efficiency adsorbents has become a research hotspot.

Iron-based adsorbents can form exosphere and endosphere complexes with As(V) owing to their abundant hydroxyl functional groups [15]. Additionally, iron oxides present special characteristics of microporosity distribution and surface charging, facilitating the adsorption of organoarsenicals, while preventing other ions or compounds in the sewage water from interfering with the adsorbent [16]. Consequently, iron-based materials have displayed a wide application in arsenic removal. Moreover, previous research has indicated that binary metal oxides and bimetallic oxides display higher adsorption capabilities compared to pure monometallic iron-based oxides [17]. MnFe_2O_4 , for instance, not only boasts strong magnetic properties, facilitating separation from solution and reducing the risk of secondary environmental pollution, but also displays better biocompatibility and lower biotoxicity [18]. The low manufacturing cost and simple preparation process of MnFe_2O_4 have garnered significant attention. As a result, MnFe_2O_4 can be considered a suitable alternative to iron-based materials. However, single MnFe_2O_4 suffers from limitations, such as restricted adsorption capacity, slow adsorption rates due to small surface areas, aggregation of active sites, and low overall adsorption efficiency, thus hindering its practical applications [19]. Graphene, a novel two-dimensional carbon material, possesses numerous outstanding properties, including a large specific surface area, strong antimicrobial characteristics, and excellent electrical and mechanical properties. While graphene can serve as an effective adsorbent for pollutants, the challenge lies in efficiently removing it from water after the treatment process [20]. To overcome this problem, an innovative technique that has received much attention is the utilization of magnetic materials for phase separation in aqueous solutions by applying a magnetic field, providing an attractive and cost-effective method for practical operation. Efforts have been made to integrate graphene with magnetic nanoparticles, and these hybridized materials can display enhanced adsorption capabilities [21].

Based on the aforementioned analysis, this research aimed to construct a MnFe_2O_4 /graphene (rGO) hybrid nanocomposite by employing a facile solvothermal method. And p-ASA and ROX were selected as the typical organoarsenicals to study the adsorption behavior. At the same time, the influence of natural environmental factors on its adsorption efficiency was explored, including ion strength, anion, humus, etc. Finally, a possible adsorption mechanism is proposed. MnFe_2O_4 /graphene-hybridized nanocomposites show

better adsorption properties for organic arsenic compared to the already reported iron-based materials, MWCNT, ZIF-8, etc. (Supplementary Table S1). This research work provides new insights for the preparation and application of new adsorbents.

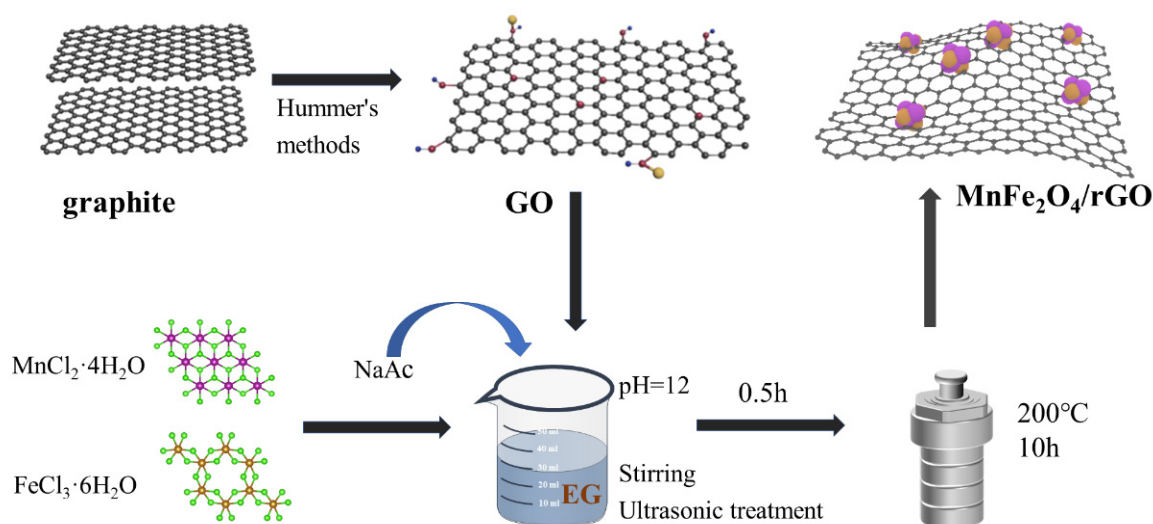
2. Materials and Methods

2.1. Reagents and Materials

Graphite was purchased from the Institute of Guangfu Chemical (Tianjin, China), and we also purchased p-arsanilic acid (Aladdin Scientific, Shanghai, China, 98%), roxarsone (Alfa Aesar, Haverhill, MA, USA, 99%), and humic acid (Sigma Aldrich, St. Louis, MO, USA). Ferric chloride hexahydrate ($\text{FeCl}_3 \cdot 6\text{H}_2\text{O}$), manganese dichloride tetrahydrate ($\text{MnCl}_2 \cdot 4\text{H}_2\text{O}$), ethylene glycol, sodium acetate anhydrous (NaAc), potassium permanganate (KMnO_4), hydrogen peroxide (H_2O_2 , 30%), concentrated sulfuric acid (H_2SO_4 , 98%), and all other chemicals were analytical reagent grade and purchased from Sinopharm Chemical Reagent Co., Ltd. (Shanghai, China), and used without further purification.

2.2. Preparation of $\text{MnFe}_2\text{O}_4/\text{rGO}$ Hybrid Nanocomposite

The graphene (rGO) was synthesized from natural graphite powder by employing a modified Hummers method. The synthesis of $\text{MnFe}_2\text{O}_4/\text{rGO}$ was based on a facile one-pot solvothermal method, using $\text{FeCl}_3 \cdot 6\text{H}_2\text{O}$ and $\text{MnCl}_2 \cdot 4\text{H}_2\text{O}$ as starting materials. As depicted in Scheme 1, 0.2 g of GO, 1 g of $\text{FeCl}_3 \cdot 6\text{H}_2\text{O}$, and 0.376 g of $\text{MnCl}_2 \cdot 4\text{H}_2\text{O}$ were dispersed in 30 mL of ethylene glycol with ultrasonication for 3 h. Later, 3 g of NaAc was added, followed by stirring for 30 min. The mixture was then transferred into a 50 mL Teflon-lined stainless-steel autoclave and heated at 200°C for 10 h. Solid black product was obtained and washed several times with deionized water and ethanol and vacuum freeze-dried. Bare MnFe_2O_4 nanoparticles were also synthesized via a similar approach but in the absence of GO. Also, barely reduced grapheme oxide denoted G was prepared under the same hydrothermal conditions but without MnFe_2O_4 nanoparticles.



Scheme 1. Schematic illustration of the formation process for $\text{MnFe}_2\text{O}_4/\text{rGO}$ hybrid nanocomposite.

2.3. Characterization

The X-ray diffractograms (XRDs) of the catalysts were analyzed using a Shimadzu XRD-6100 X-ray diffractometer (Kyoto, MA, Japan) with $\text{Cu-K}\alpha$ rays as the X-ray emission source, and the scan range was $5\text{--}80^\circ$, with a scan rate of 5°min^{-1} . Nitrogen adsorption–desorption experiments of the samples were performed on a TriStar II 3020 specific surface and porosity analyzer (Atlanta, MA, USA), and the specific surface area of the samples was calculated using Brunauer–Emmett–Teller (BET) simulations. Transmission electron microscopy (TEM) was used to observe the microstructure of the materials. The samples

were dispersed in anhydrous ethanol before testing, 1~2 drops of the suspension were placed on the carbon film, and the carbon film was fixed after the ethanol evaporated and was tested. The infrared spectra of the samples were obtained via an analysis with a Nicolet iS50 infrared spectrometer (Madison, MA, USA) with KBr as the background, scanning wavelengths of 4000–400 cm^{-1} , and spectral resolution of 4 cm^{-1} . X-ray photoelectron spectroscopy (XPS) analysis was performed by using an ESCALAB 250Xi from Thermo Scientific (Waltham, MA, USA), using XPSPEAK version 41 software for background deduction and peak splitting.

2.4. Adsorption Study

In this adsorption experiment, 20 mL of p-ASA and ROX, each with concentrations of 50 mg/L, were individually prepared. Subsequently, 20 mg of $\text{MnFe}_2\text{O}_4/\text{rGO}$ adsorbent was added to each solution. The two solutions were subjected to agitation in a shaker at 160 revolutions per minute for varying durations: 1, 3, 5, 10, 30, 60, 180, 240, 720, and 1440 min. Samples were collected, allowed to stand, passed through a membrane, and analyzed. On an Agilent 1200 HPLC (Santa Clara, MA, USA) equipped with a C18 reversed-phase column with a detection wavelength of 264 nm, the mobile phases were water and acetonitrile, the flow rate was 1 mL min^{-1} , and the injection volume was 10 L; the concentrations of p-ASA and ROX were determined. When analyzing the concentration of p-ASA, the water: acetonitrile ratio was 90:10; however, when analyzing the concentration of ROX, the ratio was 80:20. Experiments on the thermodynamics of adsorption were conducted at concentrations of 10, 25, 50, 75, and 100, 150, and 200 mg/L, with the temperature of the shaker set at 15, 25, and 35 $^\circ\text{C}$, respectively. The adsorption equilibrium may be determined using Formula (1):

$$q_e = (C_0 - C_e) \frac{V}{m} \quad (1)$$

where C_0 is the initial concentration of p-ASA or ROX (mg L^{-1}), C_e is the concentration of p-ASA or ROX when it reaches adsorption equilibrium (mg L^{-1}), V is the volume of solution added (L), and m is the mass of catalyst (g).

Different ionic intensities were adjusted to 0.01 M, 0.005 M, and 0.001 M with NaNO_3 concentrations, and 0.1 M HNO_3 or 0.1 M NaOH solution was adjusted to 3, 4, 5, 6, 7, 8, 9, and 10; different anion interference experiments were added to 0.01 M NaNO_3 , NaCl , Na_2SO_4 , and Na_3PO_4 , respectively; and the pH value of the solution was adjusted to 3, 4, 5, 6, and 7 with 0.1 M HNO_3 or 0.1 M NaOH solution. A certain concentration of HA (0, 5, 20, and 100 mg/L) was added to the humic acid interference experiment; the pH value of the solution was adjusted to 3, 4, 5, 6, 7, 8, 9, and 10 with 0.1 M HNO_3 or 0.1 M NaOH solution; and the shaker was shaken for 1440 min at a shaker speed of 160 r/min, sampled, left standing, passed through the membrane, and left standing for analysis.

3. Results and Discussion

3.1. Properties of $\text{MnFe}_2\text{O}_4/\text{rGO}$ Hybrid Nanocomposite

Figure 1a,b reveal that monomeric MnFe_2O_4 nanoparticles exhibit a circular appearance and form an aggregated microspheres distribution. Additionally, the MnFe_2O_4 microspheres are densely packed, creating porous microspheres composed of relatively large nanoparticles with average cluster size diameters ranging from 200 to 400 nm. In contrast, Figure 1d depicts a transmission electron microscopy image of the synthesized $\text{MnFe}_2\text{O}_4/\text{rGO}$, where it is evident that the MnFe_2O_4 microspheres are uniformly immobilized on transparent folded graphene sheets without significant clustering. Importantly, a large number of MnFe_2O_4 particles remain tightly bound to rGO despite ultrasonication during the preparation of TEM samples, indicating the mechanical stability of the material, which implied that the graphene structure facilitates the prevention of microsphere agglomeration and the formation of strong forces between rGO and MnFe_2O_4 [22]. These findings were consistent with those reported in the literature (Figure 1b) [23]. Furthermore, high-resolution transmission electron microscopy (HRTEM) images of both the MnFe_2O_4

and MnFe₂O₄/rGO composites reveal that the stripes with an interfacial distance of 0.3 nm correspond well to MnFe₂O₄ (220) (Figure 1c,f), confirming the successful synthesis of our composite materials.

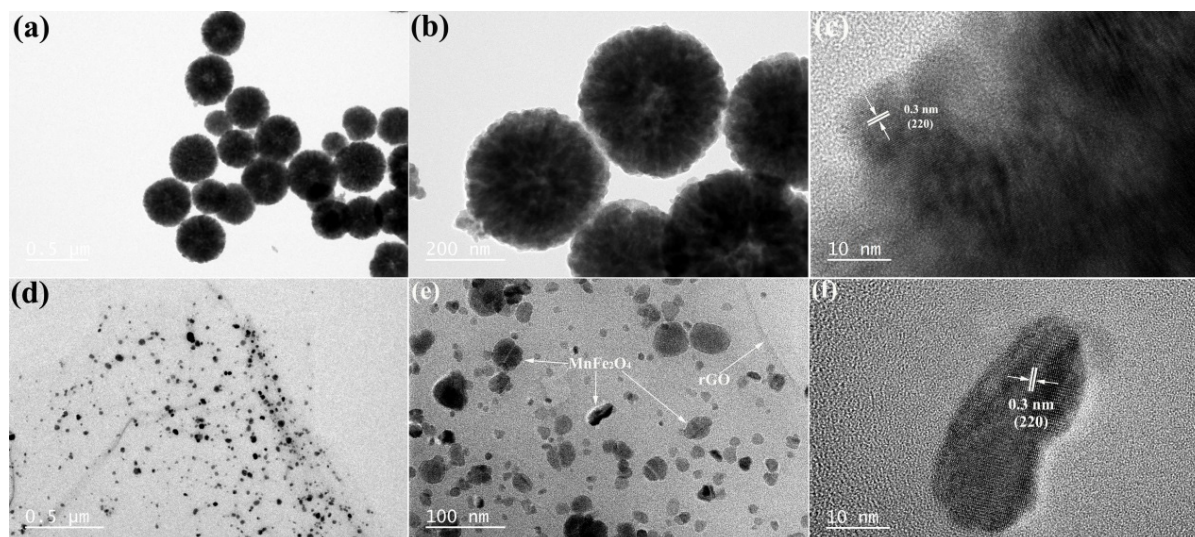


Figure 1. TEM images and high-resolution TEM images of MnFe₂O₄ (a–c) and MnFe₂O₄/rGO (d–f).

The composed MnFe₂O₄ nanoparticles were characterized by XRD, as shown in Figure 2. The XRD patterns of MnFe₂O₄ nanoparticles could well match the diffraction peaks of cubic spinel-type MnFe₂O₄ (JCPDS card No. 10-0319, space group: Fd3m, *a* = 8.50 Å) [24]. In comparison with the existing literature, rGO shows the absence of the 9.7° peak associated with the GO (001) crystal plane. This absence is attributed to the removal of oxygen-containing functional groups situated between the GO layers during the solvothermal treatment, triggering a reduction reaction that narrows the D spacing according to Bragg's law. As a result, the interlayer spacing undergoes a significant reduction, closely resembling that of rGO [25]. The characteristic diffraction peak at $2\theta = 24.5^\circ$ (002) typically observed in rGO is conspicuously absent in the as-prepared adsorbent. This absence may be attributed to the infiltration of MnFe₂O₄ nanoparticles into the reduced GO layer, causing their separation [26]. Furthermore, the diffraction peaks of MnFe₂O₄ crystals closely match those of MnFe₂O₄/rGO, indicating that the material is adequately loaded, and the diffraction peak is well-defined and sharpened. The emergence of the strongest diffraction peak of MnFe₂O₄ particles at $2\theta = 35.86^\circ$ further validates the formation of nanoparticles and their robust crystallization and growth along the crystal plane (311) [27]. The average grain size, calculated using the Scherrer formula based on the strongest peak (311), is approximately 29.7 nm.

A nitrogen adsorption–desorption analysis was employed to evaluate the specific surface area and pore size distribution of both monomeric MnFe₂O₄ and MnFe₂O₄/rGO composites (Figure 3a,b). Utilizing the BET method for nitrogen adsorption and desorption data, the specific surface areas of MnFe₂O₄ and MnFe₂O₄/rGO nanocomposites were determined to be 86.15 and 146.39 m² g^{−1}, respectively. This improvement can be attributed to the uniform distribution of MnFe₂O₄ nanoparticles on the rGO sheet. According to the IUPAC classification, the nitrogen adsorption–desorption isotherms and textural properties of MnFe₂O₄ nanoparticles exhibit a type IV hysteresis loop, which is characteristic of typical mesoporous materials [28]. In contrast, MnFe₂O₄/rGO displays a type IV H3 hysteresis loop [27], indicating the prevalence of mesoporosity and the interconnection between disordered mesoporosity and interparticle mesoporosity. It is well established that the large specific surface area and abundant mesoporous structure of the adsorbent are essential factors contributing to the improved adsorption capacity of the material for reactants [29].

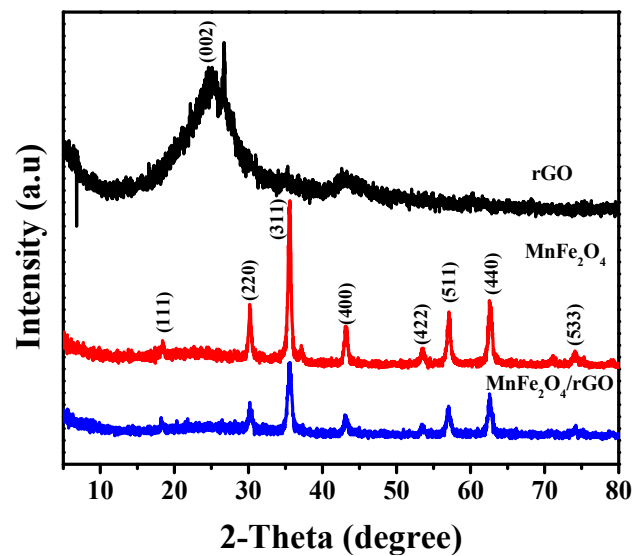


Figure 2. XRD patterns of rGO, MnFe_2O_4 , and $\text{MnFe}_2\text{O}_4/\text{rGO}$.

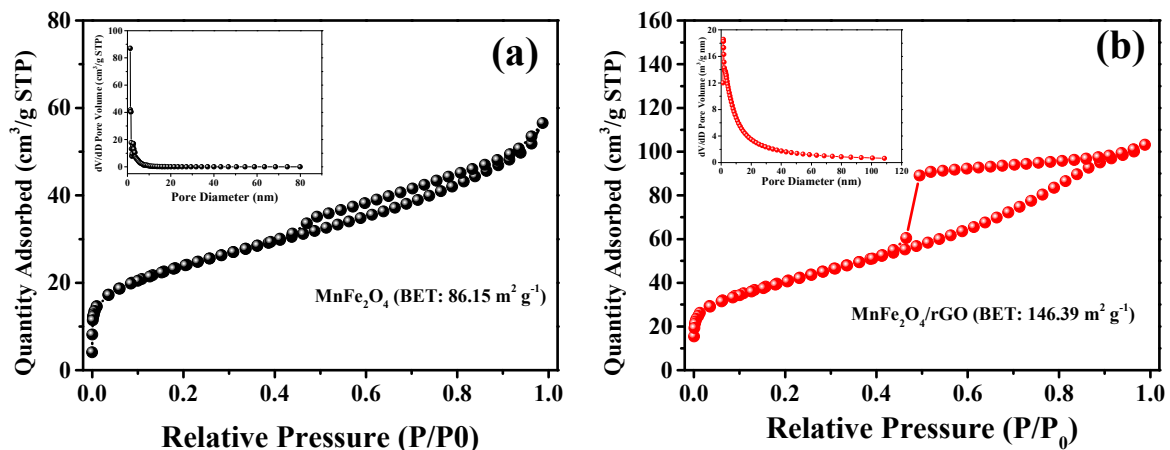


Figure 3. Nitrogen adsorption–desorption isotherms and pore diameter distribution of MnFe_2O_4 (a) and $\text{MnFe}_2\text{O}_4/\text{rGO}$ (b).

3.2. Adsorption Kinetic and Isotherms

Kinetic experiments were conducted to analyze the adsorption properties of the prepared materials for arsenic in water. Figure 4a,c illustrate the examination of adsorption kinetics for various organic arsenic species on MnFe_2O_4 particles. Active adsorption was observed for both p-ASA and ROX within the initial 100 min of the experiment. Specifically, the $\text{MnFe}_2\text{O}_4/\text{rGO}$ complex achieved the removal of 58% of the maximum adsorption capacity for p-ASA and 87% of the maximum adsorption capacity for ROX. Subsequently, between 180 and 300 min, the process continued at a relatively slow rate until equilibrium was reached around 1400 min. In addition, the adsorption rate of the $\text{MnFe}_2\text{O}_4/\text{rGO}$ complex was positively correlated with the adsorption rate of rGO and MnFe_2O_4 . This is due to the fact that MnFe_2O_4 loading onto rGO does not agglomerate, and it is also due to the intrinsic adsorption capacity of graphene itself; the combination of the two does not impair their properties, thus elucidating the enhanced adsorption capacity of the complex [30]. Notably, the adsorption of ROX by rGO was more significant. This was perhaps attributed to the presence of more nitroarsenic adsorption sites than aminoarsenic in the adsorption of contaminants by rGO. The presence of vacancies and small pores on the surface of rGO, which can provide additional adsorption sites for nitroaromatic compounds, also resulted in a substantially larger adsorption of ROX by $\text{MnFe}_2\text{O}_4/\text{rGO}$ [31].

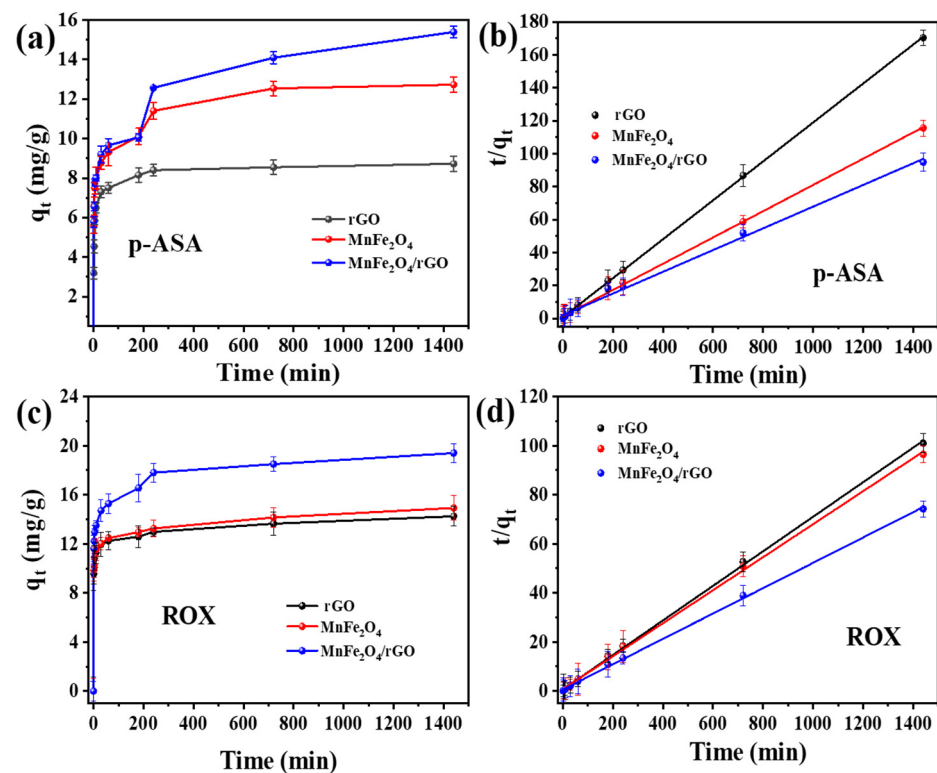


Figure 4. Adsorption performance of various samples for p-ASA (a) and ROX (c) removal. The dynamic simulation for p-ASA and ROX adsorption onto various samples: (b,d) pseudo-second-order model.

To confirm the evolving behavior of the adsorbent over the course of the adsorption process, we utilized a pseudo-second-order equation (Equation (2)) to characterize the adsorption of organic arsenic on both the monomer $MnFe_2O_4$ and the composite adsorbent.

$$\frac{t}{q_t} = \frac{1}{kq_e^2} + \frac{1}{q_e}t \quad (2)$$

where k ($g\ mg^{-1}\ min^{-1}$) is the rate constant of adsorption, and q_t ($mg\ g^{-1}$) and q_e ($mg\ g^{-1}$) are the adsorption capacity at any time and at equilibrium. The initial sorption rate, h , can be classified as shown in Equation (3):

$$h = kq_e^2(t \rightarrow 0) \quad (3)$$

The h ($mg\ g^{-1}\ min^{-1}$) and k ($g\ mg^{-1}\ min^{-1}$) values can be obtained from the slope and intercept of the t/q_t curve. The h and k were calculated for the adsorption of arsenic by $MnFe_2O_4$ in accordance with the fitted secondary kinetic model ($R^2 > 0.99$). Based on the h and k values, it was shown that the order of the initial adsorption rates of both adsorbed p-ASA and ROX obeyed $rGO < MnFe_2O_4 < MnFe_2O_4/rGO$.

The adsorption isotherm model elucidates the interaction between adsorbate and adsorbent under equilibrium conditions with a constant pH value. In an equilibrium state characterized by a constant pH value, the adsorption isotherm model is employed to characterize the interaction between the adsorbate and the adsorbent. The analysis of adsorption isotherm data aimed to evaluate the impact of temperature on the adsorption of diverse organic arsenic loads onto $MnFe_2O_4/rGO$ and to estimate the maximum adsorption capacity of the adsorbent. The depicted adsorption isotherms of ROX and p-ASA on $MnFe_2O_4/rGO$ at three different temperatures are shown in Figure 5a,d. Under the same adsorption conditions, the adsorption capacities of ROX and p-ASA are in the following order: $308K >$

298K > 288K. With the rising temperature, the equilibrium absorption increases, suggesting the endothermic character of the adsorption process. At the highest temperature (308K), the maximum adsorption capacities for ROX and p-ASA were 22.4 mg/g and 29.3 mg/g, respectively, indicating a relative advantage in the adsorption of ROX.

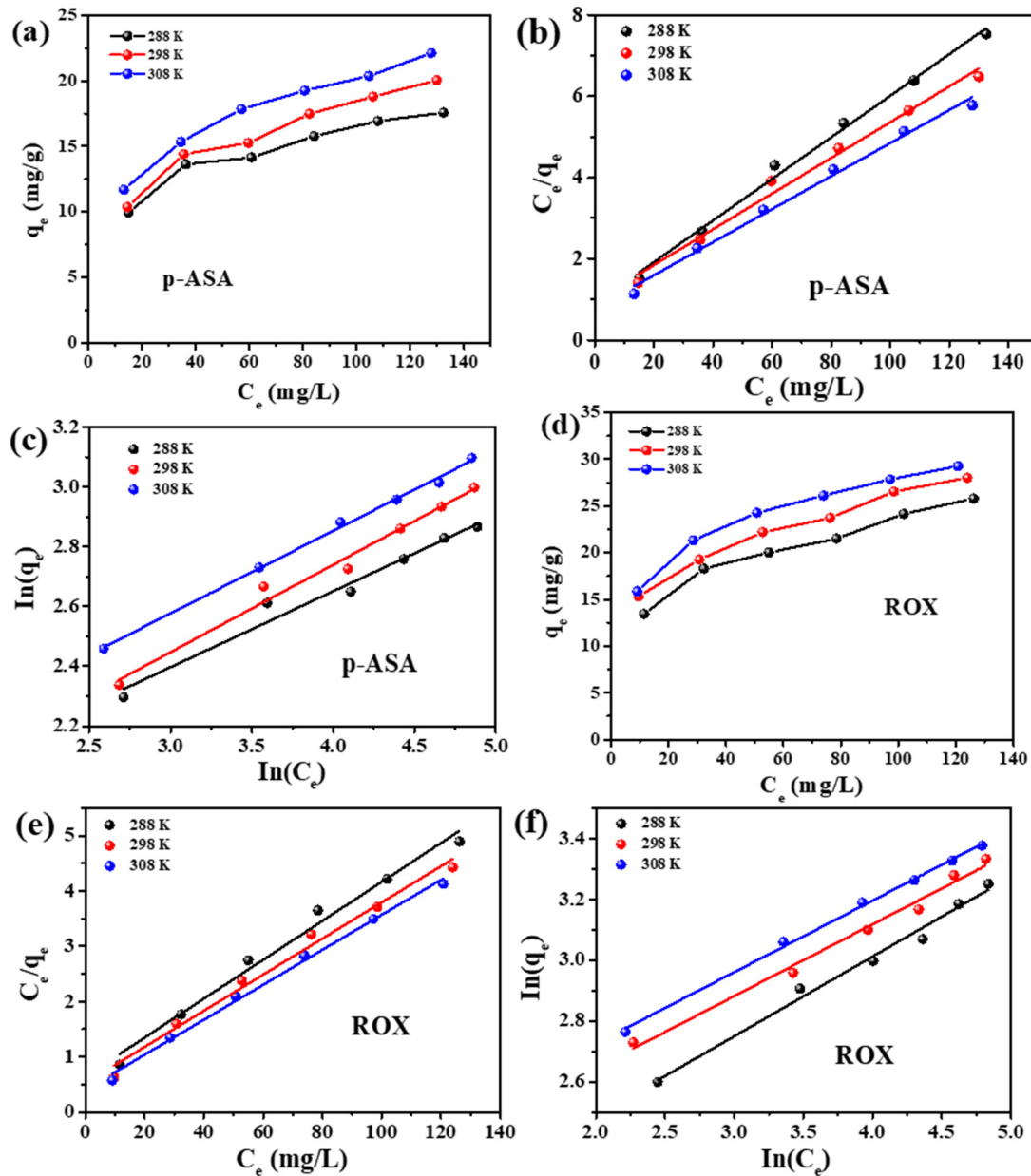


Figure 5. Adsorption isotherms for p-ASA (a) and ROX (d) adsorption on MnFe₂O₄/rGO hybrid nanocomposite, Langmuir fit (b,e), and Freundlich fit (c,f).

The equilibrium adsorption isotherm data were analyzed using the Langmuir and Freundlich isotherm models, and the following are the respective Equations (4) and (5).

$$\text{Langmuir equation : } q_e = \frac{K_{ad}q_{max}C_e}{1+K_{ad}C_e} \quad (4)$$

$$\text{Freundlich equation : } q_e = k_F C_e^{1/n} \quad (5)$$

In the presented equations, K_L (mg g^{-1}) represents the Langmuir adsorption equilibrium constant, q_m stands for the maximum adsorption capacity at monolayer coverage (mg g^{-1}), and q_e represents the amount of p-ASA and ROX adsorbed at equilibrium (mg g^{-1}). Additionally, K_F ($(\text{mg g}^{-1}) (\text{L mg}^{-1})^{1/n}$) and n are the Freundlich characteristic constants. To assess the goodness of fit and the degree of error for the validation of the isotherm model, the regression coefficient (R^2) is employed.

The Langmuir isotherm model assumes that the adsorbate forms a monolayer on the adsorbent surface, and the resulting equation describes the equilibrium between the two phases. The Freundlich isotherm model is employed based on the multilayer adsorption of adsorbates on heterogeneous surfaces. Parameters pertinent to the calculated isotherms are provided in Table S2, and the fitting curves for the expected isotherm models at the three temperatures are depicted in Figure 5b,c,e,f. Both the Langmuir and Freundlich adsorption isotherm models effectively explain the adsorption behavior of organic arsenic during the production of magnetic adsorbents, as indicated by the R^2 , all of which exceed 0.97.

By employing the Langmuir dimensionless constant separation factor (RL) [23], we can theoretically demonstrate the favorable nature of the adsorption process for organic arsenic and $\text{MnFe}_2\text{O}_4/\text{rGO}$. RL values greater than 1 suggest an unfavorable type of isotherm, while values between 0 and 1 indicate a favorable type, as expressed in Equation (6) below.

$$R_L = \frac{1}{1 + K_L C_e} \quad (6)$$

where C_e is the equilibrium concentration of adsorbate (mg L^{-1}), and K_L is the Langmuir constant. The calculated values are shown in Table S3.

The adsorption of organic arsenic onto the $\text{MnFe}_2\text{O}_4/\text{rGO}$ composite was shown to be temperature-independently advantageous, with RL values ranging from 0.686 to 0.767 ($0 < R_L < 1$).

According to the calculation of Langmuir adsorption isotherm, the maximum adsorption capacity of p-ASA and ROX on $\text{MnFe}_2\text{O}_4/\text{rGO}$ was 24.6 mg g^{-1} and 31.62 mg g^{-1} , respectively, and the maximum adsorption capacity of p-ASA and ROX at 298 K was 22.75 mg g^{-1} and 30.59 mg g^{-1} , respectively.

3.3. Effect of pH and Ionic Strength

Natural aqueous environmental media typically contain a variety of different compounds, which can potentially interfere with the adsorption process of target ions. These ions may either enhance or hinder the adsorption of organic arsenicals. Therefore, investigating the impact of ionic strength and other ions on the adsorption process can provide valuable insights into the mechanisms of adsorption. Initially, the effect of varying the concentration of NO_3^- (0.01 M, 0.005 M, and 0.001 M) was investigated, and it is observed from Figure 6a,b that the ionic strength variation has limited and almost no effect on the adsorption of p-ASA and ROX, thus suggesting that the organic arsenicals form an inner sphere complex on the $\text{MnFe}_2\text{O}_4/\text{rGO}$ surface, thereby avoiding competition with other ions [32].

3.4. Effect of Background Anions

Competition with naturally occurring anions in aquatic environments can affect the adsorption of arsenic. Therefore, four common anions (Cl^- , NO_3^- , SO_4^{2-} , and PO_4^{3-}) were chosen to investigate their influence on the $\text{MnFe}_2\text{O}_4/\text{rGO}$ adsorption process [32]. Intriguingly, 0.01 M concentrations of Cl^- , NO_3^- , and SO_4^{2-} ions at different pH levels had minimal effects on p-ASA and ROX adsorption. The removal efficiency of the two organic arsenic compounds remained at approximately 90% of their initial rates. The PO_4^{3-} anions had a significant impact on the adsorption of p-ASA and ROX, leading to a reduction in the removal of organic arsenic by 50–75%. Phosphorus and arsenic are both nonmetals belonging to the VA group and share similar chemical characteristics. It has been reported that both phosphate and arsenate are tetrahedral anions, and phosphate can potentially

form inner-sphere complexes with hydroxyl groups on the adsorbent surface, unlike other ions [33,34]. Similar results have been reported in numerous studies, indicating that the presence of phosphate effectively reduces the adsorption of arsenic compounds by metal oxides [35,36]. Regarding Cl^- , NO_3^- , and SO_4^{2-} , which have a minor inhibitory effect on adsorption, this is attributed to diffusion-based outer-sphere complexation adsorption. This suggests that the absence of electrostatic interactions has a minimal effect on the adsorption capacity.

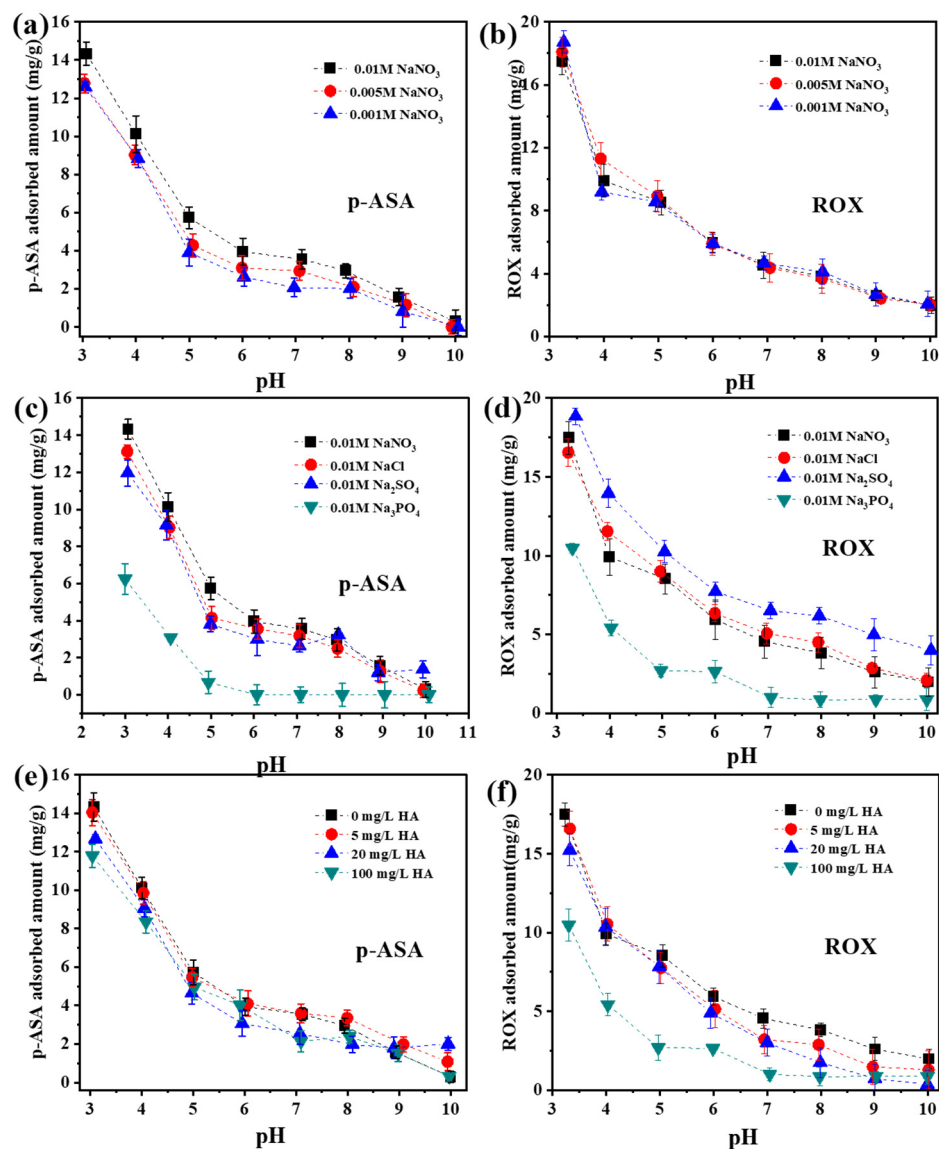


Figure 6. Effect of ionic strength (a,b), different anions (c,d), and humic acid (e,f) on the adsorption of p-ASA and ROX onto MnFe₂O₄/rGO hybrid nanocomposite.

3.5. Effect of HA

Groundwater systems with elevated arsenic levels are distinguished by a substantial concentration of dissolved organic matter. This organic matter governs the transport and transformation of contaminants within these systems, playing a pivotal role in the release of pollutants. In this context, we employed ROX and p-ASA as representative models of organic arsenicals. These compounds were subjected to adsorption studies in the presence of HA at varying concentrations of 0, 5, 20, and 100 mg·L⁻¹. As illustrated in Figure 6e,f, the adsorption of organic arsenic was impeded under the presence of p-ASA, particularly at pH values below 6, in a manner proportionate to the concentration of HA. However,

a more comparable adsorption pattern emerged at pH levels exceeding 6. In contrast, the adsorption of ROX was progressively suppressed across the entire pH range with the increasing humic acid concentration. Distinct concentrations of humic acid similarly imposed inhibitory effects on the adsorption of organic arsenic, particularly at a lower pH level.

The elemental composition and valence states of $\text{MnFe}_2\text{O}_4/\text{rGO}$ were analyzed both before and after adsorption, using XPS. In Figure 7a, the full spectrum of arsenic species is depicted before and after adsorption, with the presence of elements C, O, N, Fe, and Mn observed in all samples. Figure 7b displays the characteristic peaks of C1s. This high-resolution C1s spectrum can be deconvoluted into four peaks situated at 283.16 eV, 283.6 eV, 284.67 eV, and 287 eV, corresponding to the binding energies of C-C/C=C, C-O, C=O, and O-C=O bonds [37]. It is worth noting that the percentage content of oxygen-containing functional groups is lower compared to that reported in the literature [38]. Additionally, this finding reinforces the conclusion regarding the rGO during XRD analysis. It suggests that the conjugated π -orbital structure of graphite is disrupted, and oxygen-containing functional groups are interspersed within the graphene structure during the fabrication process [39].

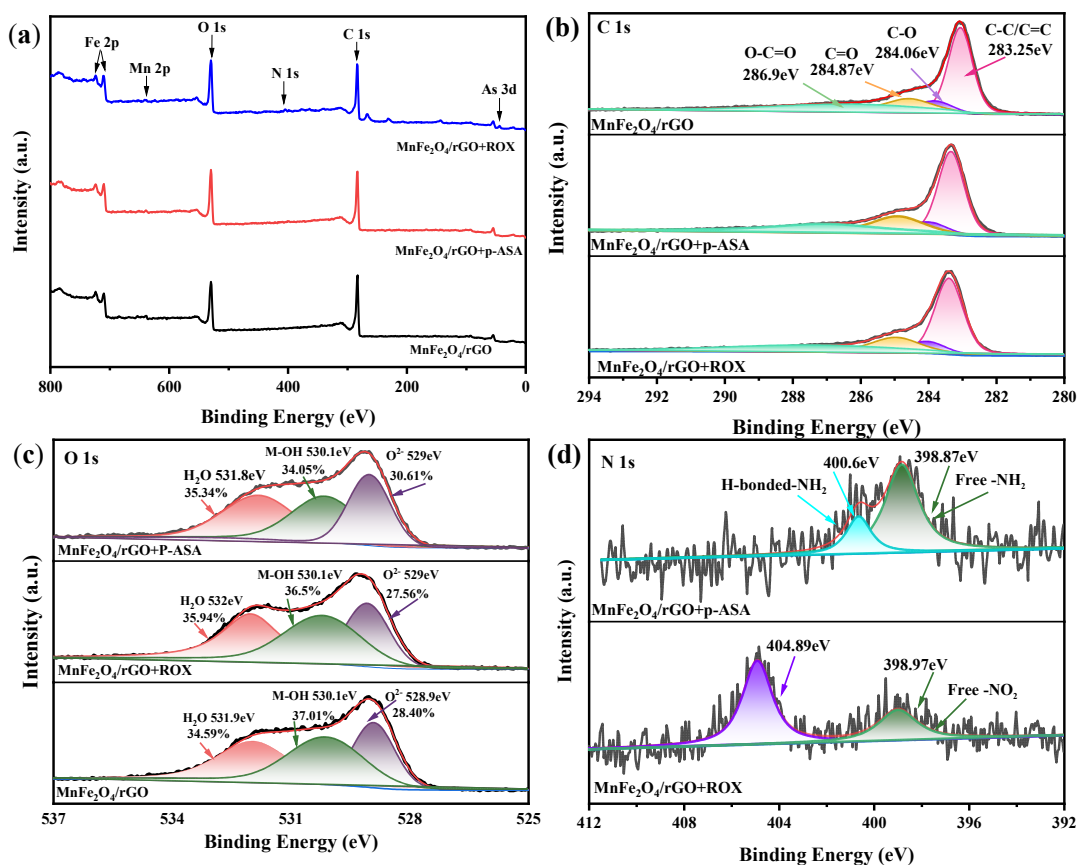


Figure 7. XPS spectra of $\text{MnFe}_2\text{O}_4/\text{rGO}$ hybrid nanocomposite before and after organoarsenic adsorption: (a) survey, (b) C 1s, (c) O 1s, and (d) N 1s.

A multi-peak Gaussian fit of $\text{MnFe}_2\text{O}_4/\text{rGO}$ before the adsorption of organic arsenic was performed to deconvolve the O 1s (Figure 7c) spectrum into three peaks centered at 528.9 eV, 530.1 eV, and 534.5 eV. The main contributions are the lattice oxygen in MnFe_2O_4 [40], the surface metal hydroxyl group (M-OH) from the oxygen-containing functional group of rGO [41], and the surface adsorbed water molecules. Significantly, the $\text{MnFe}_2\text{O}_4/\text{rGO}$ surface had a high percentage of M-OH (37.01%), which is considered to be an important component for the removal of contaminants [42]. Our experimental obser-

variations are also as expected. After adsorption of p-ASA and ROX, the oxygen-containing functional groups on the surface are less than 34.05% and 32.52%, while the O^{2-} on the surface increases from 28.40% to 30.61% and 31.50%, respectively, which may be attributed to the specific adsorption of the lattice oxygen by various arsenic species. There was a slight magnitude in the variation in the surface adsorption percentage of H_2O in $MnFe_2O_4/rGO$ prior to and following adsorption, omitting the contribution of H_2O to removal. In addition, the fact that the percentage content of M-OH is lower in the ROX-loaded $MnFe_2O_4/rGO$ in comparison to the adsorbed p-ASA indirectly means that the adsorbent facilitates the removal of ROX contaminants. In addition to electrostatic mutual interaction and surface complexation for adsorption, hydrogen bonding serves as another important principle used to explain the removal of ROX in liquid-phase adsorption. Moreover, $MnFe_2O_4/rGO$, p-ASA, and ROX in this study all have sufficient hydroxyl (-OH), amino (-NH₂), and nitro (-NO₂) to provide H-donors or H-acceptors. As shown in Figure 7d, the observation of N1s revealed the presence of hydrogen bonding after the adsorption of organic matter [43]. Crucially, bonding in hydrogen is also influenced by hydroxyl groups, and the increase in hydroxyl (-OH) groups leads to a monotonic increase in the amount of adsorbed arsenic contaminants [44], and this, combined with the above factors, is more advantageous for the removal of ROX from water.

Supplementary Figure S2 demonstrates the adsorption of p-ASA and ROX onto $MnFe_2O_4/rGO$, with peaks at 46.7 eV and 44.06 eV that are both assigned to AS^V-O [45]. This is consistent with the analysis from ATR-FTIR measurements, indicating that different forms of arsenic are adsorbed onto $MnFe_2O_4$ by forming As-O-M (M = Fe or Mn) bonds to create surface complexes [46]. Supplementary Figure S3 illustrates the adsorption of organic arsenic on this composite material, showing that the binding energy of Fe2p and Mn2p remains nearly unchanged in the chemical state before and after adsorption. This not only confirms the presence of both Fe and Mn elements in the $MnFe_2O_4/rGO$ hybrid material but also suggests that the adsorption process occurs on the surface without involving redox reactions. A slight shift in two of the peaks can be attributed to the interaction with organo-arsenic in $MnFe_2O_4/rGO$.

3.6. Adsorption Mechanism

As is well known, the zeta potential of a species is measured as a function of the pH to assess the surface's acidity or alkalinity and determine the isoelectric point (IEP). This experiment was conducted under the working conditions at pH = 3 (Supplementary Figure S4). Observations suggest that the isoelectric point (IEP) of $MnFe_2O_4/rGO$ is approximately pH = 5. Our experimental pH is lower than the protonated surface IEP of $MnFe_2O_4/rGO$, which is positively charged [47]. p-ASA and ROX can form charged species (due to the presence of acidic (nitro) and basic (amino) groups), and their pKa1 values are listed in Supplementary Figure S5. At pH = 3, both p-ASA and ROX exist in the form of molecules and mononegative ions. p-ASA has a lower pKa (1.9), indicating lower solubility, resulting in $C_6H_7AsNO_3^-$ and making up approximately 30% of the ions in solution. In contrast, ROX has a relatively higher pKa1 (3.43), with $C_6H_5AsNO_6^-$ constituting approximately 83% of the ions, and monovalent ions dominate the solution. Consequently, the adsorbent can bind organic pollutants to its surface through electrostatic attraction, thereby facilitating their removal. Additionally, the greater the hydrolysis of ROX in an aqueous solution, the higher the corresponding adsorption capacity. Moreover, considering the O fraction peak in XPS and the adsorbent's behavior in the presence of interference from other ions, we suggest the occurrence of surface complexation. Notably, post-adsorption, iron experiences a substantial shift (Supplementary Figure S3), indicating iron's involvement in the complexation reaction with organic arsenic within $MnFe_2O_4/rGO$. This leads us to speculate that a monodentate surface complexation reaction occurs with organic arsenic, resulting in a reduction in the surface hydroxyl content of $MnFe_2O_4/rGO$. This observation aligns with

the previously described FTIR analysis results regarding the formation of Fe-O-As bonds, as in Equation (7) [31,36]:



Another significant mechanism for elucidating liquid-phase adsorption is through the formation of hydrogen bonds. Since both the adsorbent and the adsorbate have hydrogen donor or hydrogen acceptor groups. The abundance of hydroxyl groups in the MnFe_2O_4 -reduced graphene oxide complex enables the formation of hydrogen bonds with the amino ($-\text{NH}_2$) or hydroxyl ($-\text{OH}$) groups present in the p-ASA molecule ($\text{O-H}\cdots\text{N}$, $\text{O-H}\cdots\text{O}$) [43]. However, in comparison with the prior literature, it was noted that the adsorption of metal oxides on organic arsenic typically results in a higher adsorption capacity for p-ASA than for ROX [19,44,48]. This difference can be attributed to the inclusion of oxygen-containing groups in the reduced graphene oxide composite prepared in this study. Nitroaromatic compounds serve as π -electron acceptors known as π -deficient aromatic molecules (NAC). The presence of oxygen-containing groups/defects/edges on the rGO surface provides electron-donating capabilities, resulting in π - π interactions beyond EDA (electron-donor-acceptor) interactions. The nitro functional groups of NAC not only enhance π - π EDA interactions but also facilitate electrostatic interactions with the oxygen-containing groups/edges/defects present in graphene materials [31] (Figure 8). $\text{MnFe}_2\text{O}_4/\text{rGO}$ retains the characteristics of reduced graphene oxide (rGO) and exhibits a heightened affinity for ROX.

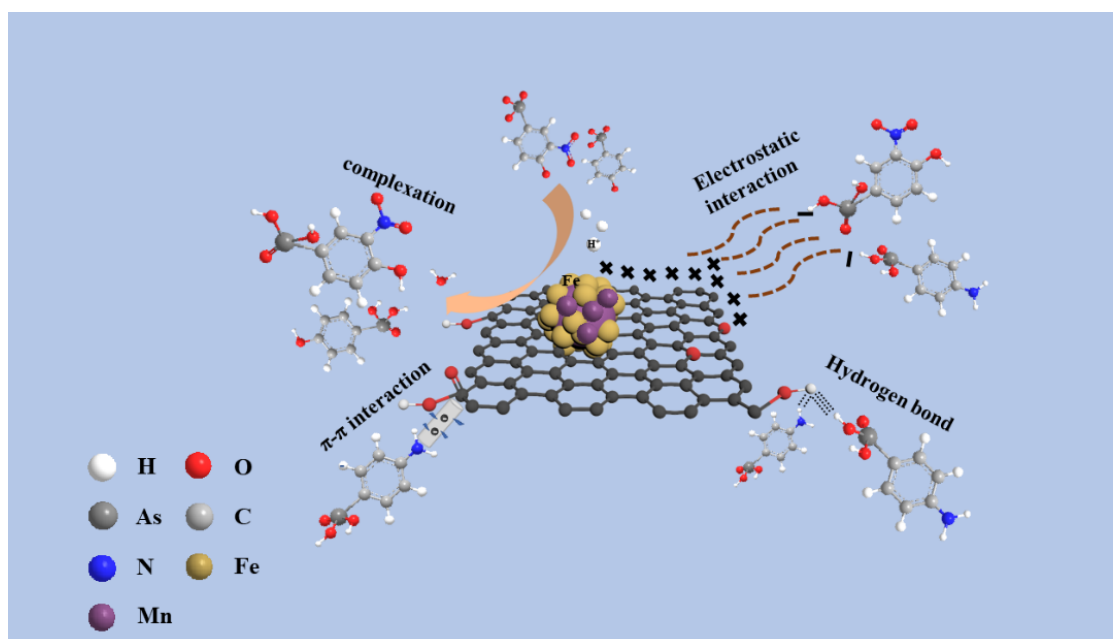


Figure 8. Possible adsorption mechanism of p-ASA and ROX over $\text{MnFe}_2\text{O}_4/\text{rGO}$ hybrid nanocomposite.

4. Conclusions

In this work, a $\text{MnFe}_2\text{O}_4/\text{rGO}$ hybrid nanocomposite was successfully synthesized via a facile solvothermal method and employed to adsorb two kinds of aromatic organoarsenic. The synergism between MnFe_2O_4 and graphene in the $\text{MnFe}_2\text{O}_4/\text{rGO}$ nanocomposite enables its high affinity towards p-ASA and ROX. The maximum adsorption capacities of p-ASA and ROX onto $\text{MnFe}_2\text{O}_4/\text{rGO}$ were 24.6 and 31.62 mg g^{-1} on account of the Langmuir adsorption isotherm. Additionally, the chemical structure of organoarsenic displays a significant impact on the adsorption capacities. Surface complexation and electrostatic interaction are the primary adsorption mechanisms on the basis of the XPS and FTIR

analysis. In general, this research shows the potential value of the MnFe₂O₄/rGO hybrid nanocomposite as a recyclable adsorbent in the purification of natural water contaminated with arsenic.

Supplementary Materials: The following supporting information can be downloaded at <https://www.mdpi.com/article/10.3390/ma16247636/s1>. Figure S1: FT-IR spectra of MnFe₂O₄ and MnFe₂O₄/rGO; Table S1: Comparison of maximum adsorption capacity (q_{max}) of p-ASA and ROX on adsorbents. Table S2: Calculated equilibrium constants for p-ASA and ROX adsorption onto MnFe₂O₄/rGO; Table S3: RL values calculated for all temperatures and concentrations; Figure S2: As 3d XPS spectra of MnFe₂O₄/rGO after p-ASA and ROX adsorption; Figure S3: Fe 2p XPS spectra and Mn 2p XPS spectra; Figure S4: pH dependent zeta-potential plots of MnFe₂O₄/rGO; Figure S5: The chemical structure formula, acidity constant and existing form in water of p-ASA (a) and ROX (b). References [49–56] are cited in the Supplementary Materials.

Author Contributions: Investigation, B.G. and H.Z.; Data curation, B.G., H.Z., M.Y. and T.Z.; Writing—original draft, B.G.; Writing—review & editing, J.Y. and Q.H.; Supervision, Q.H.; Funding acquisition, Q.H. All authors have read and agreed to the published version of the manuscript.

Funding: This work was financially supported by the Natural Science Foundation of the Jiangsu Higher Education Institutions of China (No. 22KJB610026), the China Postdoctoral Science Foundation (No. 2021M691389), and the State Key Laboratory of Pollution Control and Resource Reuse (Project No. PCRRF21036).

Institutional Review Board Statement: Not applicable.

Informed Consent Statement: Not applicable.

Data Availability Statement: The data presented in this study are available upon request from the corresponding author.

Conflicts of Interest: The authors declare no conflict of interest.

References

1. Nabi, A.; Naem, M.; Aftab, T.; Khan, M.M.A.; Ahmad, P. A comprehensive review of adaptations in plants under arsenic toxicity: Physiological, metabolic and molecular interventions. *Environ. Pollut.* **2021**, *290*, 118029. [[CrossRef](#)] [[PubMed](#)]
2. Kalami, S.; Diakina, E.; Noorbakhsh, R.; Sheidaei, S.; Rezaia, S.; Vasseghian, Y.; Kamyab, H.; Mohammadi, A.A. Metformin-modified polyethersulfone magnetic microbeads for effective arsenic removal from apatite soil leachate water. *Environ. Res.* **2024**, *241*, 117627. [[CrossRef](#)] [[PubMed](#)]
3. Schlesinger, W.H.; Klein, E.M.; Vengosh, A. The Global Biogeochemical Cycle of Arsenic. *Glob. Biogeochem. Cycles* **2022**, *36*, e2022GB007515. [[CrossRef](#)]
4. Jackson, B.P.; Bertsch, P.M. Determination of Arsenic Speciation in Poultry Wastes by IC-ICP-MS. *Environ. Sci. Technol.* **2001**, *35*, 4868–4873. [[CrossRef](#)] [[PubMed](#)]
5. Tyutereva, Y.E.; Sherin, P.S.; Polyakova, E.V.; Grivin, V.P.; Plyusnin, V.F.; Shuvaeva, O.V.; Xu, J.; Wu, F.; Pozdnyakov, I.P. Synergetic effect of potassium persulfate on photodegradation of para-arsanilic acid in Fe(III) oxalate system. *J. Photochem. Photobiol. A Chem.* **2021**, *420*, 113507. [[CrossRef](#)]
6. Polyakova, E.V.; Shuvaeva, O.V.; Koshcheeva, O.S.; Tyutereva, Y.E.; Pozdnyakov, I.P. Capillary zone electrophoresis as a simple approach for the study of p-arsanilic acid transformation in the process of photolytic degradation. *Electrophoresis* **2021**, *42*, 719–724. [[CrossRef](#)] [[PubMed](#)]
7. Zhao, D.; Wang, J.; Yin, D.; Li, M.; Chen, X.; Juhasz, A.L.; Luo, J.; Navas-Acien, A.; Li, H.; Ma, L.Q. Arsanilic acid contributes more to total arsenic than roxarsone in chicken meat from Chinese markets. *J. Hazard. Mater.* **2020**, *383*, 121178. [[CrossRef](#)]
8. Xie, X.; Hu, Y.; Cheng, H. Rapid degradation of p-arsanilic acid with simultaneous arsenic removal from aqueous solution using Fenton process. *Water Res.* **2016**, *89*, 59–67. [[CrossRef](#)]
9. Peng, M.; Guan, G.; Deng, H.; Han, B.; Tian, C.; Zhuang, J.; Xu, Y.; Liu, W.; Lin, Z. PCN-224/rGO nanocomposite based photoelectrochemical sensor with intrinsic recognition ability for efficient p-arsanilic acid detection. *Environ. Sci. Nano* **2019**, *6*, 207–215. [[CrossRef](#)]
10. Rathi, B.S.; Kumar, P.S. A review on sources, identification and treatment strategies for the removal of toxic Arsenic from water system. *J. Hazard. Mater.* **2021**, *418*, 126299. [[CrossRef](#)]
11. Giri, D.D.; Srivastava, N.; Ruidas, B.C.; Areeshi, M.Y.; Haque, S.; Pal, D.B. Bioremediation of organoarsenic pollutants from wastewater: A critical review. *Biomass Convers. Biorefinery* **2023**, *13*, 13357–13367. [[CrossRef](#)]
12. Akha, N.Z.; Salehi, S.; Anbia, M. Removal of arsenic by metal organic framework/chitosan/carbon nanocomposites: Modeling, optimization, and adsorption studies. *Int. J. Biol. Macromol.* **2022**, *208*, 794–808. [[CrossRef](#)]

13. Tian, L.; Li, H.; Chang, Z.; Liang, N.; Wu, M.; Pan, B. Biochar modification to enhance arsenic removal from water: A review. *Environ. Geochem. Health* **2023**, *45*, 2763–2778. [[CrossRef](#)]
14. Renu; Agarwal, M.; Singh, K. Heavy metal removal from wastewater using various adsorbents: A review. *J. Water Reuse Desalination* **2016**, *7*, 387–419.
15. Bataineh, H.; Pestovsky, O.; Bakac, A. Electron Transfer Reactivity of the Aqueous Iron(IV)–Oxo Complex. Outer-Sphere vs. Proton-Coupled Electron Transfer. *Inorg. Chem.* **2016**, *55*, 6719–6724. [[CrossRef](#)]
16. Ahmaruzzaman, M. Magnetic nanocomposite adsorbents for abatement of arsenic species from water and wastewater. *Environ. Sci. Pollut. Res.* **2022**, *29*, 82681–82708. [[CrossRef](#)]
17. McCann, C.M.; Peacock, C.L.; Hudson-Edwards, K.A.; Shrimpton, T.; Gray, N.D.; Johnson, K.L. In situ arsenic oxidation and sorption by a Fe-Mn binary oxide waste in soil. *J. Hazard. Mater.* **2018**, *342*, 724–731. [[CrossRef](#)]
18. Akhlaghi, N.; Najafpour-Darzi, G. Manganese ferrite (MnFe₂O₄) Nanoparticles: From synthesis to application -A review. *J. Ind. Eng. Chem.* **2021**, *103*, 292–304. [[CrossRef](#)]
19. Joshi, T.P.; Zhang, G.; Jefferson, W.A.; Perfilov, A.V.; Liu, R.; Liu, H.; Qu, J. Adsorption of aromatic organoarsenic compounds by ferric and manganese binary oxide and description of the associated mechanism. *Chem. Eng. J.* **2017**, *309*, 577–587. [[CrossRef](#)]
20. Ali, I.; Basheer, A.A.; Mbianda, X.Y.; Burakov, A.; Galunin, E.; Burakova, I.; Mkrtychyan, E.; Tkachev, A.; Grachev, V. Graphene based adsorbents for remediation of noxious pollutants from wastewater. *Environ. Int.* **2019**, *127*, 160–180. [[CrossRef](#)] [[PubMed](#)]
21. Montoro-Leal, P.; García-Mesa, J.C.; Morales-Benítez, I.; García de Torres, A.; Vereda Alonso, E. Semiautomatic method for the ultra-trace arsenic speciation in environmental and biological samples via magnetic solid phase extraction prior to HPLC-ICP-MS determination. *Talanta* **2021**, *235*, 122769. [[CrossRef](#)] [[PubMed](#)]
22. Sahoo, S.; Sahoo, P.K.; Sharma, A.; Satpati, A.K. Interfacial polymerized RGO/MnFe₂O₄/polyaniline fibrous nanocomposite supported glassy carbon electrode for selective and ultrasensitive detection of nitrite. *Sens. Actuators B Chem.* **2020**, *309*, 127763. [[CrossRef](#)]
23. Ueda Yamaguchi, N.; Bergamasco, R.; Hamoudi, S. Magnetic MnFe₂O₄-graphene hybrid composite for efficient removal of glyphosate from water. *Chem. Eng. J.* **2016**, *295*, 391–402. [[CrossRef](#)]
24. Zhang, X.-J.; Wang, G.-S.; Cao, W.-Q.; Wei, Y.-Z.; Liang, J.-F.; Guo, L.; Cao, M.-S. Enhanced Microwave Absorption Property of Reduced Graphene Oxide (RGO)-MnFe₂O₄ Nanocomposites and Polyvinylidene Fluoride. *ACS Appl. Mater. Interfaces* **2014**, *6*, 7471–7478. [[CrossRef](#)]
25. Zhang, G.; Shu, R.; Xie, Y.; Xia, H.; Gan, Y.; Shi, J.; He, J. Cubic MnFe₂O₄ particles decorated reduced graphene oxide with excellent microwave absorption properties. *Mater. Lett.* **2018**, *231*, 209–212. [[CrossRef](#)]
26. Wang, X.; Wang, H.; Li, F.; Hu, X.; Xie, Z.; Hua, T. Activation of peroxymonosulfate in an electrochemical filter by MnFe₂O₄-rGO electro-assisted catalytic membrane for the degradation of oxytetracycline. *J. Environ. Chem. Eng.* **2022**, *10*, 107008. [[CrossRef](#)]
27. Wei, Z.; Huang, S.; Zhang, X.; Lu, C.; He, Y. Hydrothermal synthesis and photo-Fenton degradation of magnetic MnFe₂O₄/rGO nanocomposites. *J. Mater. Sci. Mater. Electron.* **2020**, *31*, 5176–5186. [[CrossRef](#)]
28. Kruk, M.; Jaroniec, M. Gas adsorption characterization of ordered organic-inorganic nanocomposite materials. *Chem. Mater.* **2001**, *13*, 3169–3183. [[CrossRef](#)]
29. Di, J.; Xia, J.; Ge, Y.; Xu, L.; Xu, H.; He, M.; Zhang, Q.; Li, H. Reactable ionic liquid-assisted rapid synthesis of BiOI hollow microspheres at room temperature with enhanced photocatalytic activity. *J. Mater. Chem. A* **2014**, *2*, 15864–15874. [[CrossRef](#)]
30. Chella, S.; Kollu, P.; Komarala, E.V.P.R.; Doshi, S.; Saranya, M.; Felix, S.; Ramachandran, R.; Saravanan, P.; Koneru, V.L.; Venugopal, V.; et al. Solvothermal synthesis of MnFe₂O₄-graphene composite—Investigation of its adsorption and antimicrobial properties. *Appl. Surf. Sci.* **2015**, *327*, 27–36. [[CrossRef](#)]
31. Chen, X.; Chen, B. Macroscopic and Spectroscopic Investigations of the Adsorption of Nitroaromatic Compounds on Graphene Oxide, Reduced Graphene Oxide, and Graphene Nanosheets. *Environ. Sci. Technol.* **2015**, *49*, 6181–6189. [[CrossRef](#)] [[PubMed](#)]
32. Barreto, M.S.C.; Elzinga, E.J.; Sparks, D.L. The adsorption of arsenate and p-arsanilic acid onto ferrihydrite and subsequent desorption by sulfate and artificial seawater: Future implications of sea level rise. *Environ. Pollut.* **2023**, *323*, 121302. [[CrossRef](#)] [[PubMed](#)]
33. Zeng, H.; Fisher, B.; Giammar, D.E. Individual and competitive adsorption of arsenate and phosphate to a high-surface-area iron oxide-based sorbent. *Environ. Sci. Technol.* **2008**, *42*, 147–152. [[CrossRef](#)] [[PubMed](#)]
34. Su, C.; Puls, R.W. Arsenate and Arsenite Removal by Zerovalent Iron: Effects of Phosphate, Silicate, Carbonate, Borate, Sulfate, Chromate, Molybdate, and Nitrate, Relative to Chloride. *Environ. Sci. Technol.* **2001**, *35*, 4562–4568. [[CrossRef](#)] [[PubMed](#)]
35. Lafferty, B.J.; Loeppert, R.H. Methyl arsenic adsorption and desorption behavior on iron oxides. *Environ. Sci. Technol.* **2005**, *39*, 2120–2127. [[CrossRef](#)] [[PubMed](#)]
36. Chen, W.-R.; Huang, C.-H. Surface adsorption of organoarsenic roxarsone and arsanilic acid on iron and aluminum oxides. *J. Hazard. Mater.* **2012**, *227–228*, 378–385. [[CrossRef](#)]
37. Chandra, V.; Park, J.; Chun, Y.; Lee, J.W.; Hwang, I.-C.; Kim, K.S. Water-Dispersible Magnetite-Reduced Graphene Oxide Composites for Arsenic Removal. *ACS Nano* **2010**, *4*, 3979–3986. [[CrossRef](#)]
38. Hassani, A.; Eghbali, P.; Mahdipour, F.; Waclawek, S.; Lin, K.Y.A.; Ghanbari, F. Insights into the synergistic role of photocatalytic activation of peroxymonosulfate by UVA-LED irradiation over CoFe₂O₄-rGO nanocomposite towards effective Bisphenol A degradation: Performance, mineralization, and activation mechanism. *Chem. Eng. J.* **2023**, *453*, 139556. [[CrossRef](#)]

39. Lian, P.; Zhu, X.; Liang, S.; Li, Z.; Yang, W.; Wang, H. Large reversible capacity of high quality graphene sheets as an anode material for lithium-ion batteries. *Electrochim. Acta* **2010**, *55*, 3909–3914. [[CrossRef](#)]
40. Rathore, R.; Waghmare, A.; Rai, S.; Chandra, V. Removal of nitrobenzene from aqueous solution using manganese ferrite nanoparticles. *Inorg. Chem. Commun.* **2023**, *153*, 110848. [[CrossRef](#)]
41. Subramanian, H.; Santhaseelan, H.; Dinakaran, V.T.; Devendiran, V.; Rathinam, A.J.; Mahalingam, A.; Ramachandran, S.K.; Muthukumarasamy, A.; Muthukumar, K.; Mathimani, T. Hydrothermal synthesis of spindle structure copper ferrite-graphene oxide nanocomposites for enhanced photocatalytic dye degradation and in-vitro antibacterial activity. *Environ. Res.* **2023**, *231*, 116095. [[CrossRef](#)] [[PubMed](#)]
42. Vences-Alvarez, E.; Chazaro-Ruiz, L.F.; Rangel-Mendez, J.R. New bimetallic adsorbent material based on cerium-iron nanoparticles highly selective and affine for arsenic(V). *Chemosphere* **2022**, *297*, 134177. [[CrossRef](#)] [[PubMed](#)]
43. Jun, J.W.; Tong, M.; Jung, B.K.; Hasan, Z.; Zhong, C.; Jhung, S.H. Effect of central metal ions of analogous metal-organic frameworks on adsorption of organoarsenic compounds from water: Plausible mechanism of adsorption and water purification. *Chem. A Eur. J.* **2015**, *21*, 347–354. [[CrossRef](#)] [[PubMed](#)]
44. Sarker, M.; Song, J.Y.; Jhung, S.H. Adsorption of organic arsenic acids from water over functionalized metal-organic frameworks. *J. Hazard. Mater.* **2017**, *335*, 162–169. [[CrossRef](#)]
45. Kumar, S.; Nair, R.R.; Pillai, P.B.; Gupta, S.N.; Iyengar, M.A.R.; Sood, A.K. Graphene Oxide–MnFe₂O₄ Magnetic Nanohybrids for Efficient Removal of Lead and Arsenic from Water. *ACS Appl. Mater. Interfaces* **2014**, *6*, 17426–17436. [[CrossRef](#)] [[PubMed](#)]
46. Haris, S.A.; Dabagh, S.; Mollasalehi, H.; Ertas, Y.N. Alginate coated superparamagnetic iron oxide nanoparticles as nanocomposite adsorbents for arsenic removal from aqueous solutions. *Sep. Purif. Technol.* **2023**, *310*, 123193. [[CrossRef](#)]
47. Rajani, M.R.; Ravishankar, R.; Maya, N.K.; Srinidhi, R.M.; Vidya, C.; Girish, K.S.; Manjunatha, C. Carbonaceous MnFe₂O₄ nano-adsorbent: Synthesis, characterization and investigations on chromium (VI) ions removal efficiency from aqueous solution. *Appl. Surf. Sci. Adv.* **2023**, *16*, 100434.
48. Hu, Q.; Liu, Y.; Gu, X.; Zhao, Y. Adsorption behavior and mechanism of different arsenic species on mesoporous MnFe₂O₄ magnetic nanoparticles. *Chemosphere* **2017**, *181*, 328–336. [[CrossRef](#)]
49. Liu, J.; Ren, S.; Cao, J.; Tsang, D.C.W.; Beiyuan, J.; Peng, Y.; Fang, F.; She, J.; Yin, M.; Shen, N.; et al. Highly efficient removal of thallium in wastewater by MnFe₂O₄-biochar composite. *J. Hazard. Mater.* **2021**, *401*, 123311. [[CrossRef](#)]
50. Al-Gaashani, R.; Najjar, A.; Zakaria, Y.; Mansour, S.; Atieh, M.A. XPS and structural studies of high quality graphene oxide and reduced graphene oxide prepared by different chemical oxidation methods. *Ceram. Int.* **2019**, *45*, 14439–14448. [[CrossRef](#)]
51. Wen, Z.; Zhang, Y.; Guo, S.; Chen, R. Facile template-free fabrication of iron manganese bimetal oxides nanospheres with excellent capability for heavy metals removal. *J. Colloid Interface Sci.* **2017**, *486*, 211–218. [[CrossRef](#)] [[PubMed](#)]
52. Joshi, T.P.; Zhang, G.; Koju, R.; Qi, Z.; Liu, R.; Liu, H.; Qu, J. The removal efficiency and insight into the mechanism of para-arsanilic acid adsorption on Fe-Mn framework. *Sci. Total Environ.* **2017**, *601–602*, 713–722. [[CrossRef](#)] [[PubMed](#)]
53. Zhang, G.-S.; Qu, J.-H.; Liu, H.-J.; Liu, R.-P.; Li, G.-T. Removal Mechanism of As(III) by a Novel Fe–Mn Binary Oxide Adsorbent: Oxidation and Sorption. *Environ. Sci. Technol.* **2007**, *41*, 4613–4619. [[CrossRef](#)]
54. Jung, B.K.; Jun, J.W.; Hasan, Z.; Jhung, S.H.J.C.E.J. Adsorptive removal of p-arsanilic acid from water using mesoporous zeolitic imidazolate framework-8. *Chem. Eng. J.* **2015**, *267*, 9–15. [[CrossRef](#)]
55. Poon, L.; Younus, S.; Wilson, L. Adsorption study of an organo-arsenical with chitosan-based sorbents. *J. Colloid Interface Sci.* **2014**, *420*, 136–144. [[CrossRef](#)]
56. Hu, J.; Tong, Z.; Hu, Z.; Chen, G.; Chen, T. Adsorption of roxarsone from aqueous solution by multi-walled carbon nanotubes. *J. Colloid Interface Sci.* **2012**, *377*, 355–361. [[CrossRef](#)] [[PubMed](#)]

Disclaimer/Publisher’s Note: The statements, opinions and data contained in all publications are solely those of the individual author(s) and contributor(s) and not of MDPI and/or the editor(s). MDPI and/or the editor(s) disclaim responsibility for any injury to people or property resulting from any ideas, methods, instructions or products referred to in the content.